Electronic Supplementary Information For:

Water Splitting with Polyoxometalate-Treated Photoanodes: Enhancing Performance through Sensitizer Design

John Fielden, Jordan M. Sumliner, Nannan Han, Yurii V. Geletii, Xu Xiang, Djamaladdin G. Musaev, Tianquan Lian and Craig L. Hill.

Contents

The electronic supplementary information has been organized in the order that items are discussed in the main paper

1. Comments on the Synthesis of H_2**2**

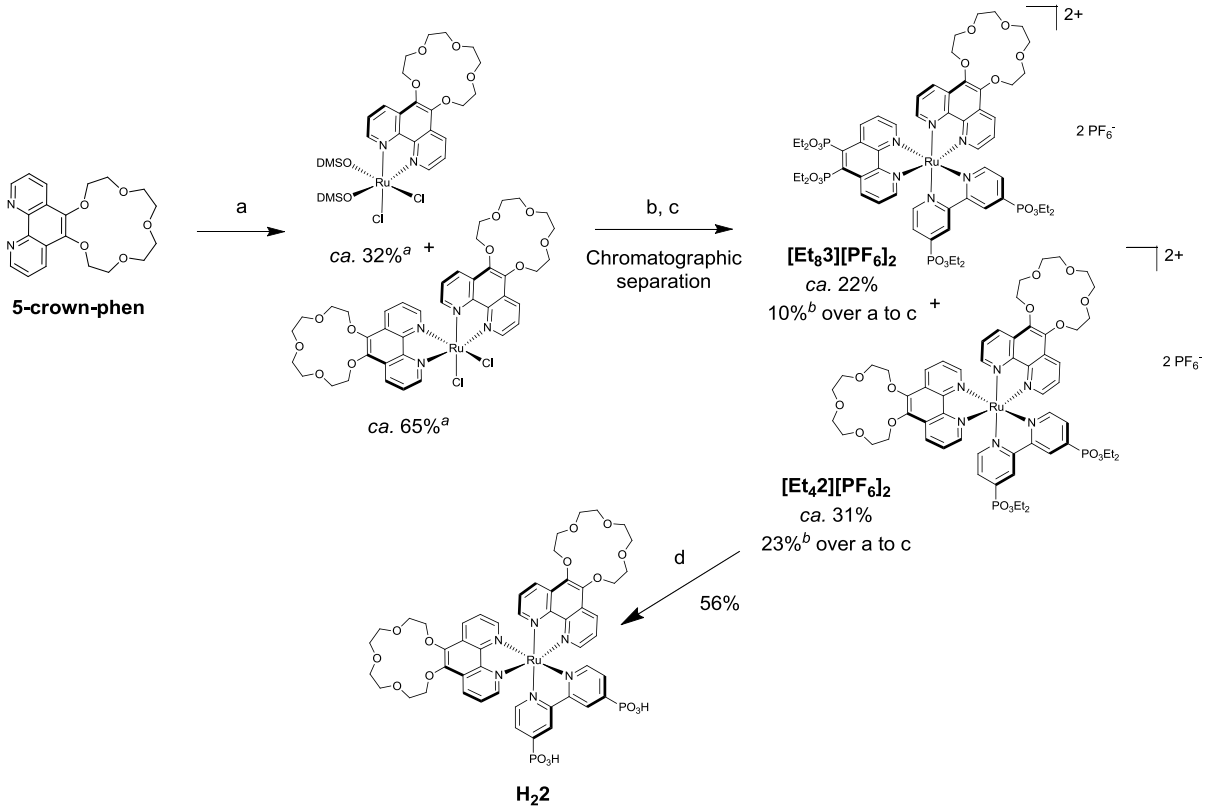

Scheme S1 Synthesis of H_2**2**. Reagents and conditions: (**a**) $Ru(DMSO)_4Cl_2$, $[NMe_4]Cl$, DMF, 120 °C, 4 h; (**b**) Et_4dpbpy, $EtOH/H_2O$, reflux, 18 h, then NH_4PF_6; (**c**) Triethylorthoacetate / MeCN, reflux, 5 h, chromatographic separation, NH_4PF_6; (**d**) 4 M $HCl_{(aq)}$, reflux, 6 h. [a]Yield for each compound estimated from ^{1}H-NMR integration and crude mass and based on $RuCl_3$. [b]Yield over steps a to c based on limiting ligand for each complex (5-crown-phen for [Et_4**2**][PF_6]$_2$, Et_4dpbpy for [Et_8**2**][PF_6]$_2$).

H_2**2** is synthesized from the 5-crown-phen ligand, with either $Ru(DMSO)_4Cl_2$ or $RuCl_3$ as the ruthenium starting material. However, we found that $RuCl_3$ resulted in large quantities of unidentified side products in the first step, whereas the lower temperature reaction facilitated by $Ru(DMSO)_4Cl_2$ cleanly produced an approximately 2:1 mixture of [Ru(5-crown-phen)$_2Cl_2$] and [Ru(5-crown-phen)$(dmso)_2Cl_2$]. Chromatographic separation of these complexes was inefficient, and adding more 5-crown-phen led to formation of *tris*-5-crown phen complexes, so the mixture was directly reacted with 4,4'-diphosphonic acid ethyl ester-2,2'-bipyridine (Et_4dbpby), before the partially hydrolysed phosphonic acid ester groups were re-esterified by treatment with triethylorthoacetate. The precursor [Et_4**2**][PF_6]$_2$ could then be chromatographically isolated before hydrolysis of the phosophonate esters to produce the target, which precipitates from water–acetone as doubly deprotonated, neutral H_2**2**. The mono-crown sister compound [(Et_4dpbpy)$_2$Ru(5-crown-phen)][PF_6]$_2$ ([Et_8**3**][PF_6]$_2$) was also isolated and characterized and will be reported upon in more detail in a future manuscript. The main source of loss in this synthesis would appear to be the chromatographic separation of [Et_4**2**][PF_6]$_2$ and [Et_8**3**][PF_6]$_2$, and potentially reprecipitation of these hydrophobic complexes from acetone-ether: the combined crude yield of [$Et_{4-x}H_x$**2**][PF_6]$_2$ and [$Et_{8-x}H_x$**3**][PF_6]$_2$ after step b is in the region of 65%.

2. Crystallographic Bond Lengths and Extended Structure

Bond Lengths. The Ru-N bond lengths and angles of H_2**2** are summarized below (Table S2). They are typical of Ru polypyridyls, the bond lengths staying within a narrow range of 2.046(4) to 2.073(4) Å, with those to the dpbpy ligand slightly shorter than those to 5-crown-phen.

Table S1 Bond lengths (Å) and angles (°) of the Ru coordination sphere of H_2**2**

Ru1-N1	2.073(4)	N1-Ru1-N3	97.4(2)
Ru1-N1A	2.073(4)	N1A-Ru1-N3	171.4(2)
Ru1-N2	2.065(4)	N1-Ru1-N3A	171.4(2)
Ru1-N2A	2.065(4)	N1A-Ru1-N3A	97.4(2)
Ru1-N3	2.046(4)	N2-Ru1-N2A	176.9(2)
Ru1-N3A	2.046(4)	N2-Ru1-N3	90.3(2)
N1-Ru1-N1A	87.2(2)	N2A-Ru1-N3	92.1(2)
N1-Ru1-N2	80.1(2)	N2-Ru1-N3A	92.1(2)
N1A-Ru1-N2	97.6(2)	N2A-Ru1-N3A	90.3(2)
N1-Ru1-N2A	97.6(2)	N3-Ru1-N3A	79.1(2)
N1A-Ru1-N2A	80.1(2)		

Extended hydrogen bonded structure. The phosphonate groups of H_2**2** lead to formation of hydrogen bonded chains of H_2**2** molecules propagating in the crystallographic *bc* plane. Further hydrogen bonds between the crown ether groups and included water molecules connect the chains into a 3D network.

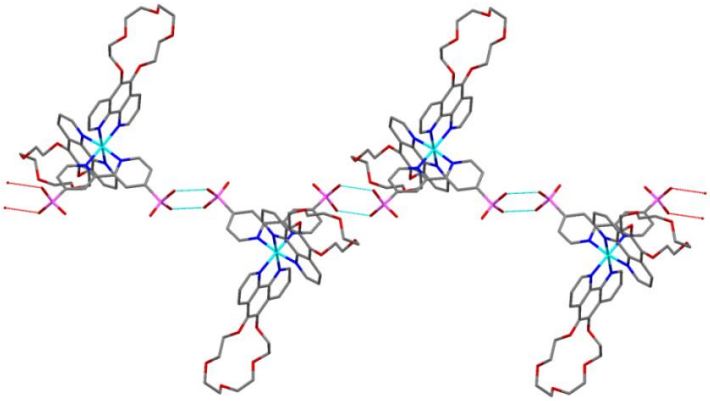

Figure S1 Hydrogen bonding between phosphonate groups in a chain of H_2**2** molecules. C atoms are grey; N, blue; O, red; P, magenta; Ru, light blue; H-bonds to solvent water molecules are omitted for clarity.

3. UV-vis spectra and Cyclic Voltammograms of $[Et_4\mathbf{2}][PF_6]_2$ in the presence and absence of cations

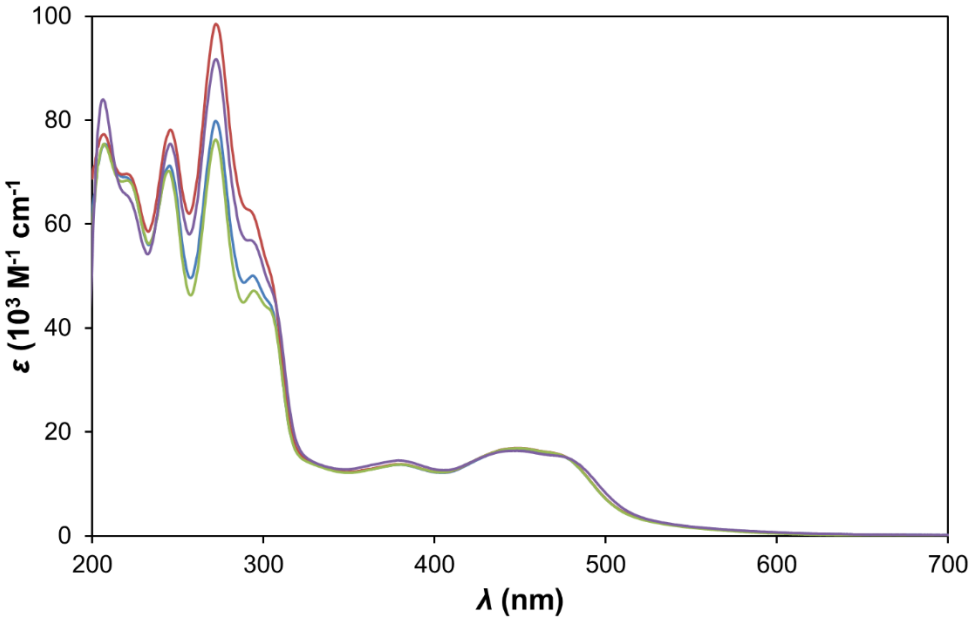

Figure S2 Effect of alkali metal cations and ionic strength (NBu_4^+) on the UV-vis spectrum of $[Et_4\mathbf{2}][PF_6]_2$. Blue, no cation added; red, $[NBu_4][PF_6]$; green, $NaClO_4$; purple, $Mg(ClO_4)_2$. In all cases 500 equivalents of salt was added to *ca.* 2 x 10^{-5} M $[Et_4\mathbf{2}][PF_6]_2$ in MeCN at 298 K.

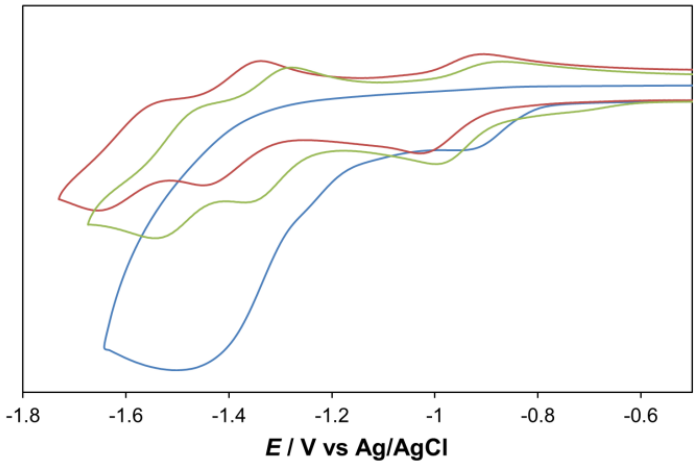

Figure S3 Effect of alkali metal cations on the ligand centered reductions of $\mathbf{[}Et_4\mathbf{2]}^{2+}$ in 0.1 M NBu_4PF_6, scan rate 125 mV s^{-1}. Red, no cation; green, Na^+; blue, Mg^{2+}. The first reduction is still reversible in the presence of Mg^{2+} if the scan direction is changed before the second two processes occur.

4. Typical UV-vis Spectra of Films: Summary of Dye and Catalyst Loadings

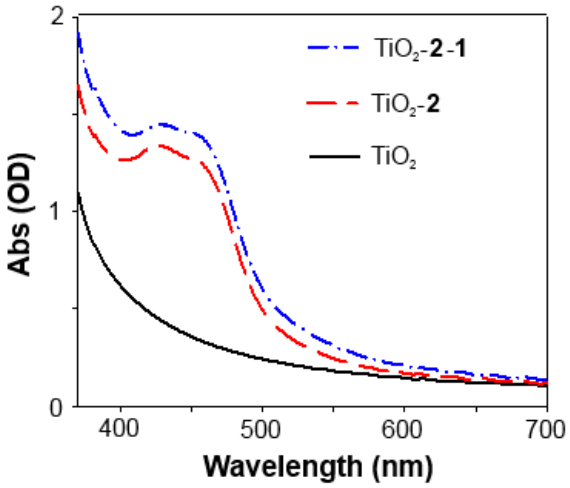

Figure S4 UV-vis absorption spectra of TiO_2 (black), TiO_2-**2** (red) and TiO_2-**2**-**1** (blue).

Differences between the absorption spectra of TiO_2, TiO_2-**dye** and TiO_2-**dye-1** (Figure S4, for TiO_2-**2**) were used to estimate loadings of the two species based on their extinction coefficients at 455 nm (11700 for **P2**, 19100 for **2** and 32000 for **1** on the TiO_2 surface). The results for films used in photoelectrochemical experiments are summarized below in Table S3:

Table S2 Loadings (nmol cm^{-2}) of dye and catalyst in assembled water oxidation triads. Loadings are based on flat surface areas, and do not take into account surface roughness.

TiO_2-P2-1 films		**TiO_2-2Na_2-1 films**	
Dye	Catalyst	Dye	Catalyst
87	10	65	12
89	13	80	11
101	19	82	14
33[a]	13	57	13
60[a]	12	42[a]	10
53[a]	10	27[a]	13
		49[a]	10

[a]Dye loading lowered by previous use in photoelectrochemical experiment as a TiO_2-**dye** dyad.

14. Ultrafast Visible TAS – Variation of Catalyst Loading and pH

Both catalyst loading and pH influence the rate of the bleach recovery of **2**.

Table S3 Summary of dye (**2**)-to-catalyst (**1**) ratios obtained for catalyst loading dependence experiments.

Experiment	Supporting dyad	Dye (**2**) : Catalyst (**1**) ratio in triad
A	TiO_2-**2**	180 : 100
B	TiO_2-**2**	90 : 100
C	TiO_2-**2**Na_2	60 : 100
D	TiO_2-**2**Na_2	40 : 100

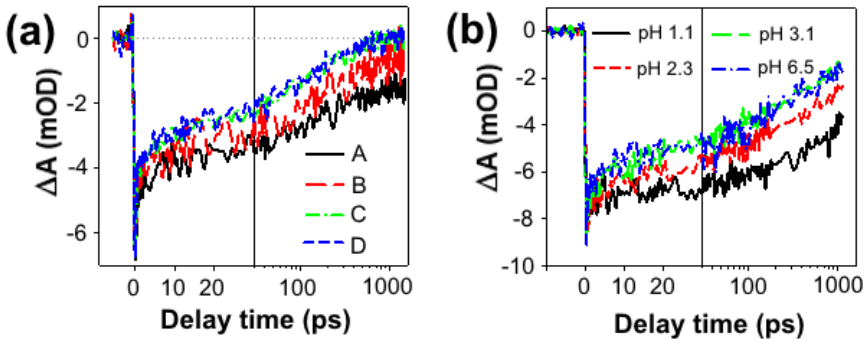

Figure S5 (a) Ground state bleach recovery of **2** in the presence of different loadings of **1** on TiO_2 (**A** – lowest loading, **D** – highest loading, see Table S4); **(b)** Comparison of the ground state recovery kinetics of TiO_2-**2**-**1**films after rinsing with different pH solutions of $HClO_4$.

6. Photoelectrochemical Control Experiments

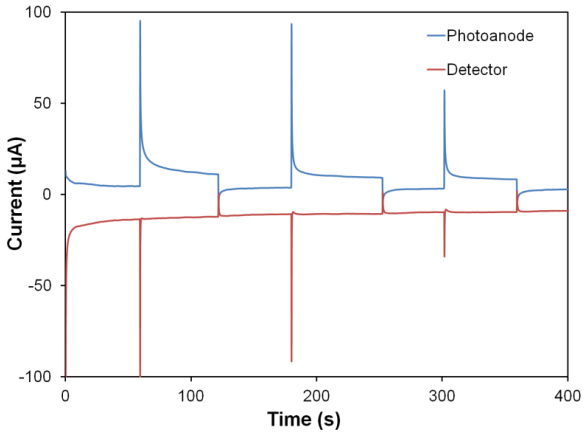

Figure S6 Photoelectrochemical generator/detector experiment conducted in acetonitrile (0.1 M in NBu_4PF_6) with a TiO_2-**P2-1** photoelectrode (at 0 V) and a plain FTO glass slide as a detector (at -0.75 V vs Ag/AgCl). Illumination (20 mW) is from a 455 nm LED. The detector response, apart from the initial spike in response to electron injection, is very small, indicating that the reduction current depends on the presence of water.

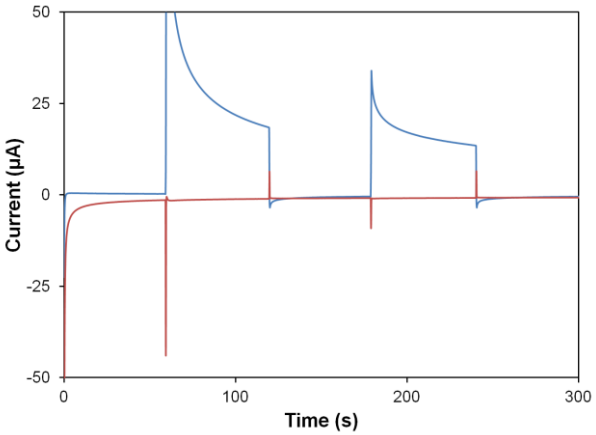

Figure S7 Photoelectrochemical generator/detector experiment at pH 7.2 with a TiO_2-**2Na$_2$-1** photoelectrode (at 0 V) and a plain FTO glass slide as a detector (-0.6 V vs Ag/AgCl). Illumination (20 mW) is from a 455 nm LED. In contrast to the platinised FTO detector films, the response is very small (< 0.1 μA) after the initial spike that results from the charging current response to electron injection at the photoanode. This shows that the pseudo-steady state photocurrent must result from reduction of a chemical species, catalysed by Pt.

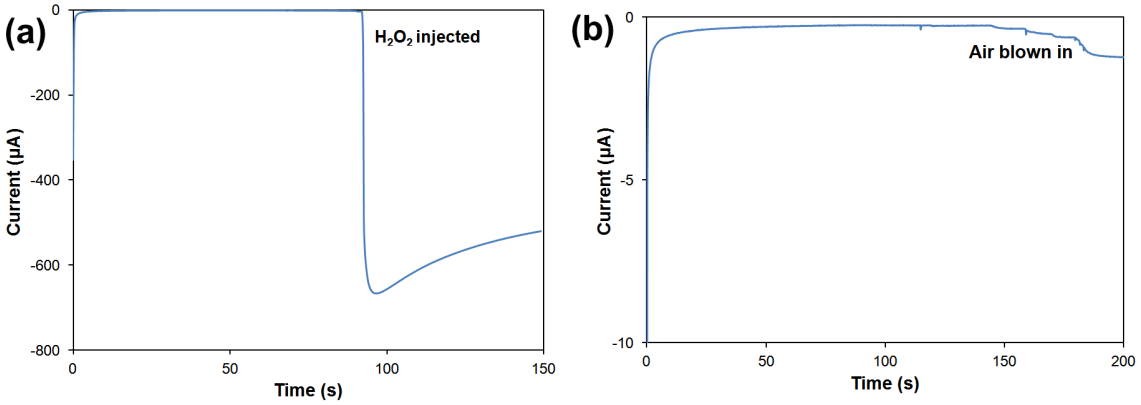

Figure S8 Control chronoamperometry experiments on an FTO slide at -0.6 V vs Ag/AgCl, in degassed lutidine buffer at pH 7.2: (**a**) One drop of H_2O_2 injected after *ca*. 90 s produces a very large current response (*ca.* 700 µA); (**b**) Air blown in in several bursts after 120 s produces a slow, and weak response (< 1 µA, note difference in scales between the two graphs). The total amount of oxygen blown in far exceeds that produced by the photoanodes. The strong response to H_2O_2, and weak response to O_2, suggests that the species generated by the photoelectrochemistry experiments cannot be H_2O_2 (or other easily reduced species such as hydroxyl radicals), but is likely to be O_2.

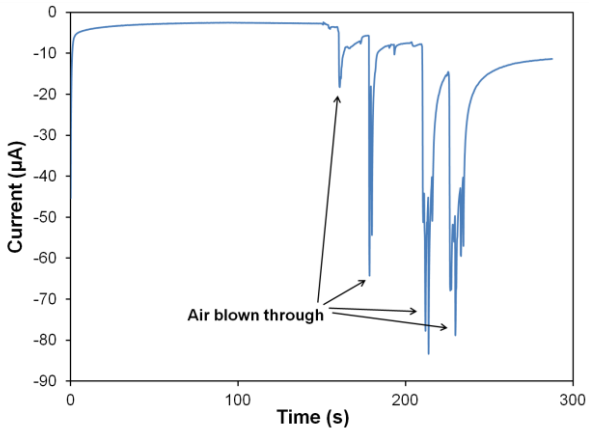

Figure S9 Chronoamperometry of a Pt@FTO film held at -0.6 V vs Ag/AgCl, in pH 7.2 lutidine buffer. Bubbling air through the buffer solution produces a very strong detector response.

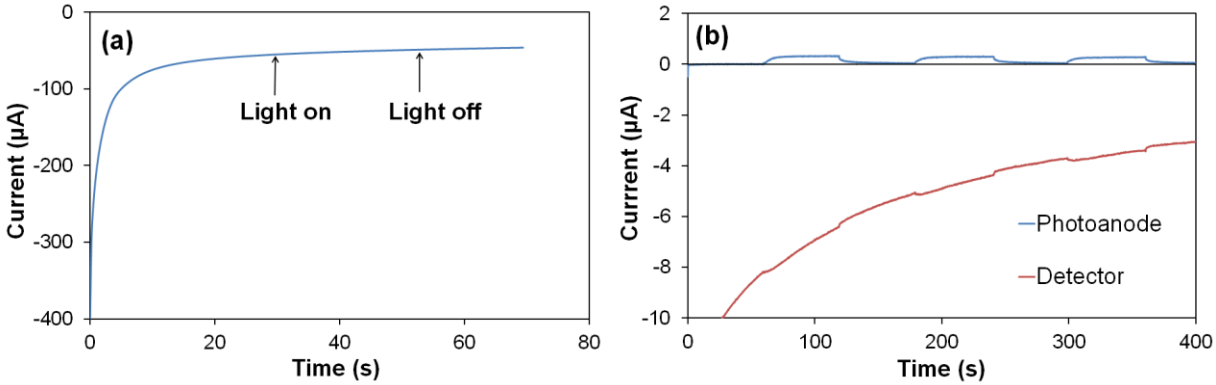

Figure S10 (a) Chronoamperometry of a Pt@FTO film held at -0.516 V vs Ag/AgCl, in pH 5.8 $Na_2SiF_6/NaHCO_3$ buffer, in the presence of $[Ru(phen)_3]^{2+}$. Irradiation of the solution (20 mW, 455 nm) produces no photocurrent response, indicating that reduction of desorbed dye cannot be a source of the detector currents. **(b)** Photoelectrochemical generator/detector experiment on a bare TiO_2 film, at pH 5.8, with photoanode at 0 V and Pt@FTO detector at -0.516 V vs Ag/AgCl. It can be seen that direct bandgap excitation of TiO_2 produces only a very small response (*ca.* 0.3 µA, an order of magnitude lower than even the P2 dyad electrodes).

7. Extended Photoelectrochemical Experiments

These were carried out to investigate the performance of the triadic photoelectrodes over several hours. Noise in the measurements carried out on the **P2** based systems has been minimized using a moving average to smooth the chronoamperometry (current vs time) plots (Figure S11b). No treatment has been used in the integrated (charge vs time plots), Figure S12.

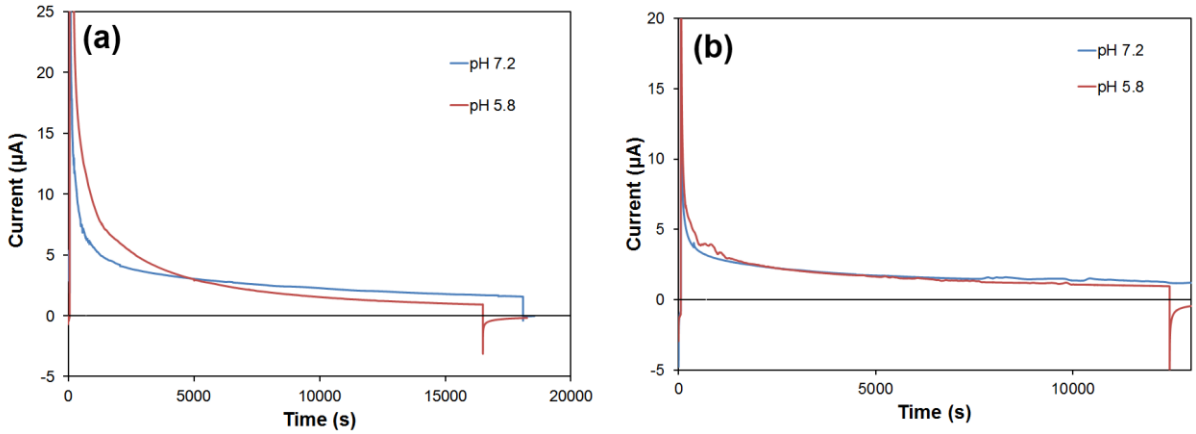

Figure S11 Photoelectrochemical (chronoamperometry) experiments at 0 mV *vs* Ag/AgCl with illumination from a 455 nm blue LED (20 mW into 0.6 cm^2): **(a)** TiO_2-**2Na$_2$-1** in pH 7.2 50 mM lutidine with 200 mM $NaClO_4$ (blue), and pH 5.8 Na_2SiF_6/$NaHCO_3$ (200 mM in Na, red); **(b)** TiO_2-**P2-1** at pH 7.2 (blue) and pH 5.8 (red). For both systems the initial photocurrent is higher at pH 5.8, but long term stability appears better in the pH 7.2 buffer.

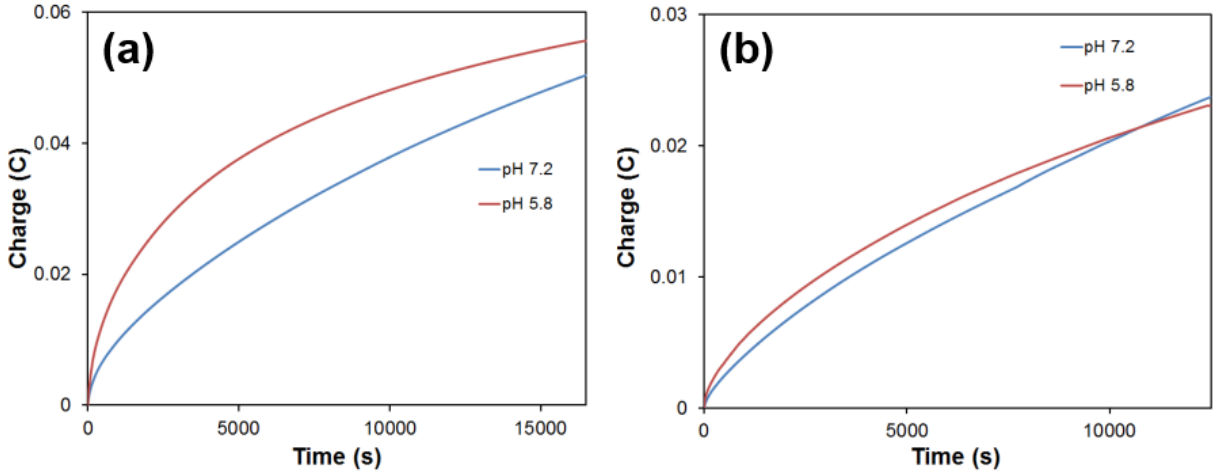

Figure S12 Bulk electrolysis (charge vs time) plots from photoelectrochemical experiments at 0 mV *vs* Ag/AgCl with illumination from a 455 nm blue LED (20 mW into 0.6 cm^2): **(a)** TiO_2-**2Na$_2$-1** in pH 7.2 50 mM lutidine with 200 mM $NaClO_4$ (blue), and pH 5.8 Na_2SiF_6/$NaHCO_3$ (200 mM in Na, red); **(b)** TiO_2-**P2-1** at pH 7.2 (blue) and pH 5.8 (red). It is clear that the early time advantage at pH 5.8 is much smaller with the **P2** sensitizer, and after about 3 hours, charge passed at pH 7.2 exceeds that at pH 5.8.

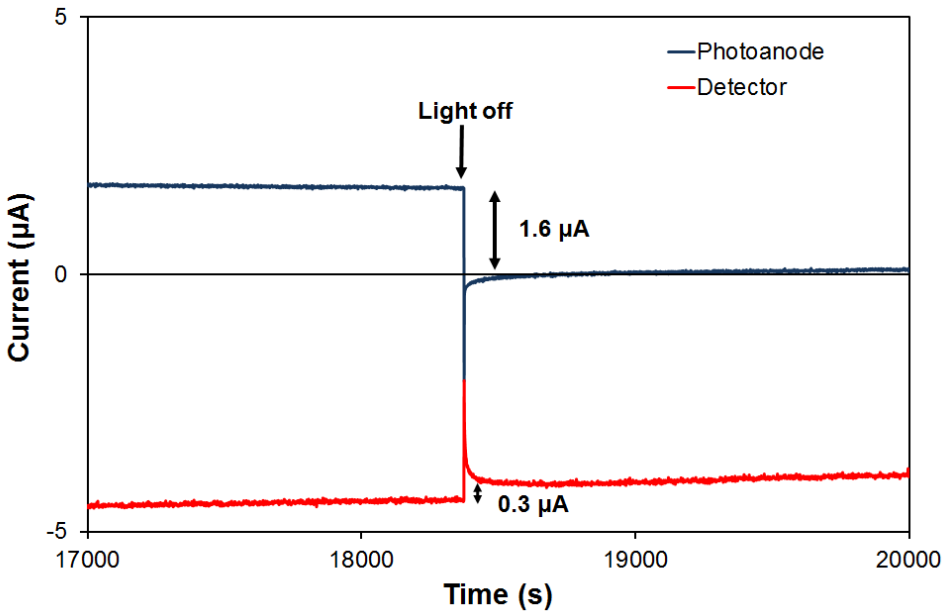

Figure S13 End of a long photoelectrochemical experiment with a Pt@FTO detector in place, with a TiO_2-**2Na$_2$-1** photoanode. The *ca*. 0.3 µA fall in detector current that accompanies the fall in photoanode current indicates that the photoanode is still producing O_2 after 5 hours. As the performance of the platinized films declines quite quickly with use, however, it is not possible to estimate a faradaic efficiency at the end of the experiment. Conditions: pH 7.2 50 mM lutidine (200 mM $NaClO_4$) 0 mV bias *vs* Ag/AgCl applied to the photoanode, -0.6 V *vs* Ag/AgCl to the detector, with illumination from a 455 nm blue LED (20 mW into 0.6 cm^2).

8. Transient Visible Spectroscopy of H$_2$**2** in Aqueous Solution

The transient absorption spectra and kinetics of H$_2$**2** in aqueous solution are shown in Figure S14. The dye has an excited state with a half-life of 685 ns in water (298 K, in the presence of O_2).

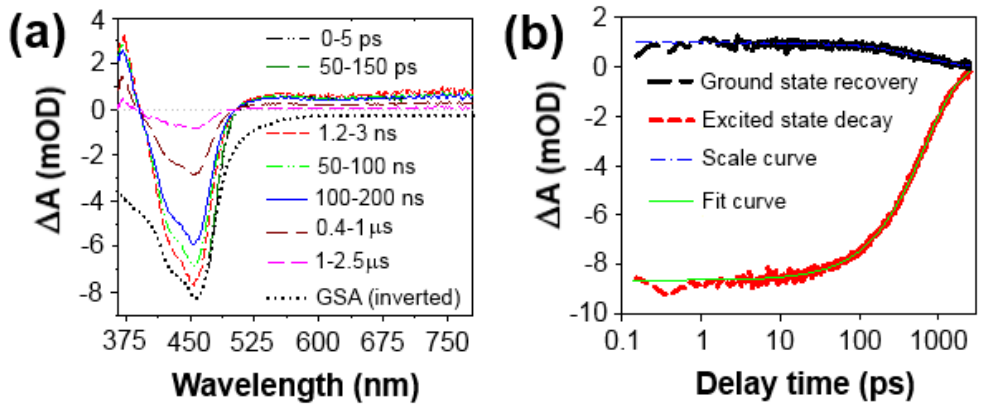

Figure S14 (a) Transient absorption spectra of H$_2$**2** in aqueous solution at indicated delay times after excitation at 400 nm. GSA is the ground-state absorption of H$_2$**2** in aqueous solution. **(b)** Kinetics of excited state decay and ground state recovery: **Red** - ground state bleach averaged over 410-480 nm; **Black** - excited state signal averaged over 570-760nm.

9. UV-vis Spectra of Dyes and Catalyst 1 at High and Low pH

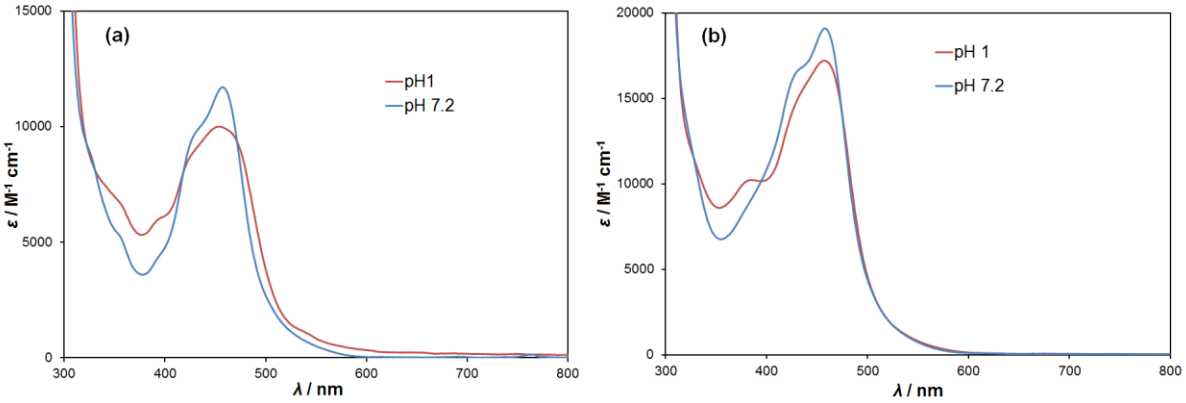

Figure S15 UV-vis spectra of the two sensitizers in a 50 mM lutidine buffer at pH 7.2 and after acidification to pH 1 by addition of H_2SO_4: **(a) P2** and; **(b) H2**.

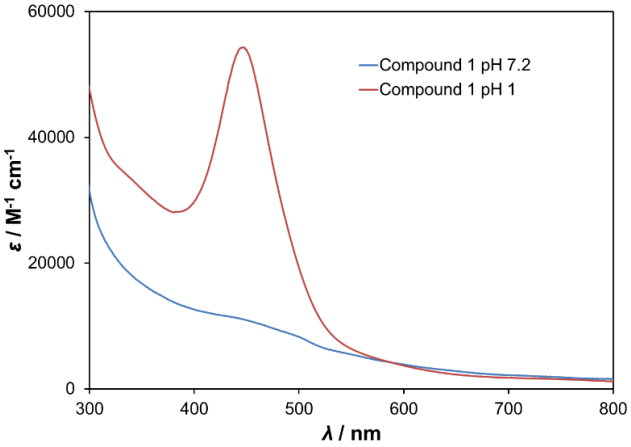

Figure S16 UV-vis spectra of **1** in 50 mM pH 7.2 lutidine (blue) buffer in pH 1 H_2SO_4 (red), showing the dramatic change in extinction coefficient with pH.

10. UV-vis Spectra of Buffers from Desorption Experiments: Calculation of lost dye and catalyst

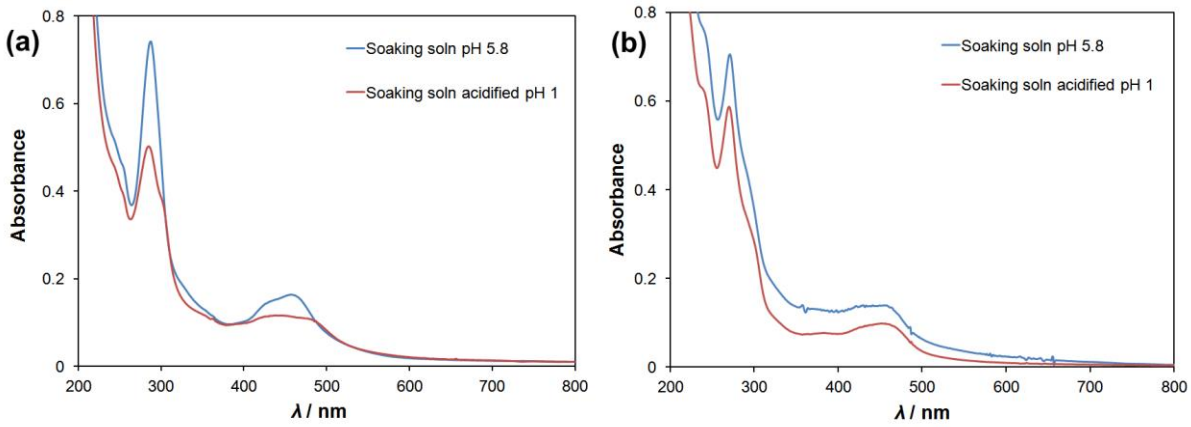

Figure S17 UV-vis spectra (after 60 minutes) of pH 5.8 $Na_2SiF_6/NaHCO_3$ buffers used to soak: **(a)** TiO_2-**P2-1** and; **(b)** TiO_2-**2-1** photoelectrodes. After measurement at the buffer pH, the solutions were acidified to pH 1 by addition of 1 drop of 98% H_2SO_4. In both examples 3 mL of buffer was used.

Figure S17 shows the spectra of solutions from desorption experiments conducted on TiO_2-**P2-1** and TiO_2-**2-Na_2-1** photoanodes in pH 5.8 buffer (Na_2SiF_6/$NaHCO_3$). In both cases, the drop in absorbance from pH 5.8 to pH 1 exceeds what would be predicted based on pH driven changes of extinction coefficient for the dye (*ca.* 15% for **P2** and 10% for **2**, Figure S17). This indicates that none of the catalyst **1** can be lost at this pH (the extinction coefficient of **1** increases dramatically upon acidification and would counterbalance the reduced absorbance from the dyes).

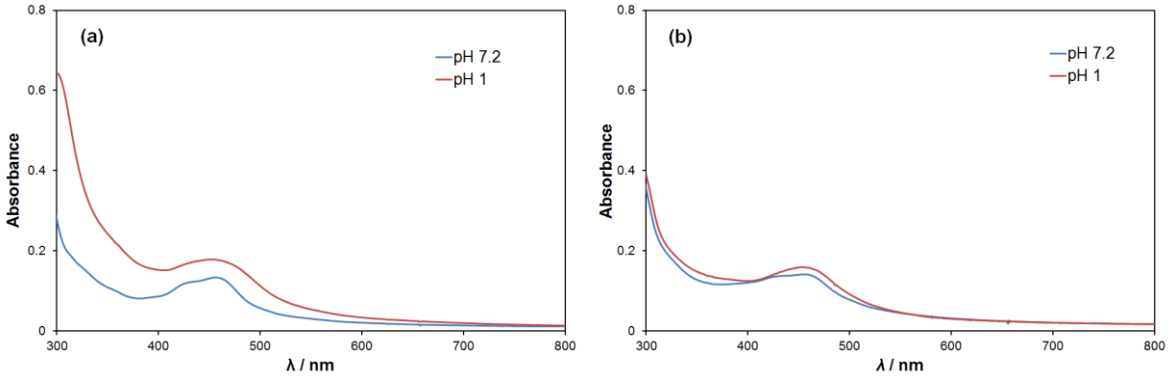

Figure S18 UV-vis spectra (after 60 minutes) of pH 7.2 lutidine buffers used to soak: **(a)** TiO_2-**P2-1** and; **(b)** TiO_2-**2-1** photoelectrodes. After measurement at the buffer pH, the solutions were acidified to pH 1 by addition of 1 drop of 98% H_2SO_4. In both examples 3 mL of buffer was used.

Figure S18 shows the spectra of solutions from desorption experiments conducted on TiO_2-**P2-1** and TiO_2-**2Na_2-1** photoanodes in pH 7.2 lutidine buffer. In both cases, an increase in absorbance is observed upon acidification from pH 7.2 to pH 1 – and the increase is larger for the **P2** based photoelectrodes. As it is known that the extinction coefficient of **1** increases dramatically at low pH (Fig. S16), this indicates that **1** is lost from both photoelectrodes, but that the losses are less severe with the crown derivatized dye **2**. To get the quantitative data presented in Table 6 of the paper, we followed the iteration procedure below, demonstrated for TiO_2-**P2-1**:

P2: ε_{455} = 11700 at pH 7.2; 10000 at pH 1, $\Delta\varepsilon_{455}$ = 1700
1: ε_{455} =10700 at pH 7.2, 52000 at pH 1, $\Delta\varepsilon_{455}$ = 41300

At pH 7.2, Abs_{455} = 0.133
At pH 1, Abs_{455} = 0.178
ΔAbs_{455} = 0.045

To make initial estimate of concentration of **1**, assume extinction coefficient of dye is constant and divide ΔAbs_{455} by , $\Delta\varepsilon_{455}${**1**}. The path length of the cuvette is 1 cm so:

$0.045/(41300\ M^{-1}\ cm^{-1} \times 1\ cm) = 1.09 \times 10^{-6}$ M

At pH 7.2, this will contribute an absorbance of 1.09×10^{-6} M × 10700 M^{-1} cm^{-1} × 1 cm = 0.0117

The remaining Abs_{455}: 0.133 – 0.0117 = 0.1213 results only from the dye **P2**. This will decrease upon acidification:

0.1213 × (10000/11700) = 0.1037 at pH 1

Refined catalyst contribution to pH 1 Abs_{455} = 0.178 – 0.1037 = 0.0743

Refined catalyst concentration = $0.0743/(52000\ M^{-1}\ cm^{-1} \times 1\ cm) = 1.429 \times 10^{-6}$ M

This procedure is repeated a second time, inserting the calculated concentration of catalyst at pH 1 back in at pH 7.2, to get a refined estimate of the quantity of dye and catalyst lost from the photoelectrode.

11. Evolution of Photoelectrode Absorbance Loss with Time

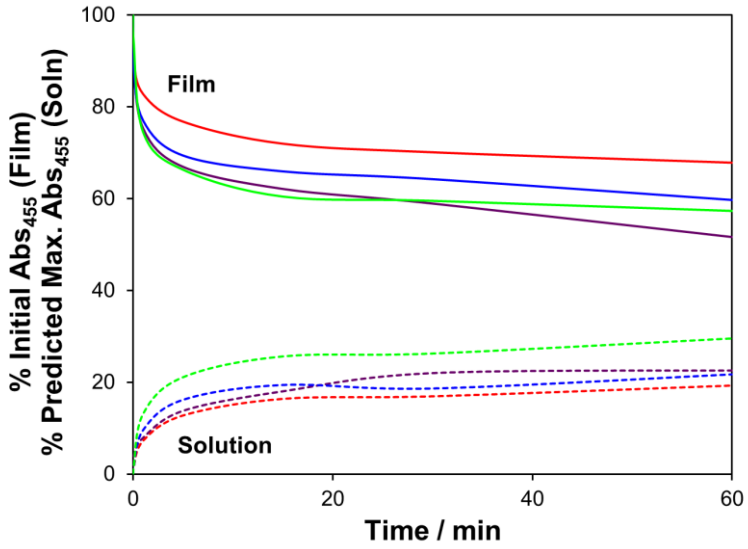

Figure S19 Desorption of TiO_2-**2-1** and TiO_2-**P2**-1 films into 50 mM lutidine / 200 mM $NaClO_4$ pH 7.2 buffer. Solid lines show the absorbance of each film over time as a percentage of the initial value (TiO_2 background subtracted). Dashed lines show the absorbance of the solution over time, as a percentage of the predicted maximum based on the initial film absorbance. Purple, **P2**; red, **2**; blue, **2-Na_2**; green, **2-Mg_2**.

12. Experimental Details

12.1 Synthesis

Materials and Procedures. All synthetic manipulations in the synthesis of H_2**2** were carried out under an inert atmosphere (Argon) using standard Schlenk techniques. Polyoxometalate chemistry (TBA_7H_3[**1**]) was carried out under air. TiO_2 colloids were prepared according to a modified literature method.[1] $Rb_8K_2[\{Ru_4O_4(OH)_2(H_2O)_4\}\gamma\text{-}SiW_{10}O_{36})_2]\bullet 25H_2O$ (Rb_8K_2[**1**])[2] and $THpA_{8.5}H_{1.5}[\{Ru_4O_4(OH)_2(H_2O)_4\}(\gamma\text{-}SiW_{10}O_{36})_2]$ ($THpA_{8.5}H_{1.5}$[**1**]),[3] 5-crown-phen,[4] 2,2'-bipyridine-4,4'-diphosphonic acid ethyl ester (Et_4dpbpy),[5] $[Ru(bpy)_2(dpbpy)]Cl_2$ (**P2**)[6] and $Ru(DMSO)_4Cl_2$[7] were all prepared using established methods. Platinized FTO films were obtained by heat treatment of $H_4[PtCl_6]$ deposited on FTO from ^{i}PrOH, following a literature procedure.[8] Several treatments were needed to produce highly responsive films. Anhydrous DMF was purchased from EMD in *Drisolv*® bottles. All other chemicals were bought as ACS reagent grade from commercial sources and used as received.

Structural Characterization. NMR spectra were acquired using Varian INOVA 400 and Bruker Avance 300 spectrometers and all shifts are quoted with respect to TMS. The fine splitting of pyridyl or phenyl ring AA'BB' patterns is ignored and the signals are reported as simple doublets. Mass spectra were acquired using a Thermo LTQ-FTMS at the Emory University Mass Spectrometry Center, or outsourced to the UK EPSRC National Mass Spectrometry Facility in Swansea, UK. FTIR spectra were acquired using Nicolet FTIR 6700 and PerkinElmer Spectrum Two instruments. Elemental analyses (CHN) were performed by Atlantic MicroLab, Inc and by London Metropolitan University. X-ray diffraction data (see below) were obtained using a Bruker Apex II CCD diffractometer (Cu K_α, λ = 1.54178 Å).

Synthesis of [(Et$_4$dpbpy)Ru(5-crown-phen)$_2$](PF$_6$)$_2$ ([Et$_4$2][PF$_6$]$_2$). 5-crown-phen (68 mg, 0.183 mmol) was added to a mixture of Ru(DMSO)$_4$Cl$_2$ (50 mg, 0.103 mmol) and tetramethylammonium chloride (250 mg, 0.428 mmol) in dry DMF (5 mL). After stirring at 130 °C for 4 hours, the mixture was cooled and added to DCM (80 mL) and precipitated tetramethylammonium chloride was removed by filtration. The filtrate was washed with 3 × 40 mL portions of water before drying over MgSO$_4$ and evaporation to yield a crude purple solid (84 mg) which was shown by ^{1}H-NMR to contain an approximately 2:1 mixture of [Ru(5-crown-phen)$_2$Cl$_2$] and [Ru(5-crown-phen)Cl$_2$(solv)$_2$] products. Without further purification, this was combined with Et$_4$dpbpy (66 mg, 0.154 mmol) in EtOH 9:1 H$_2$O (20 mL), and refluxed for 18 hours taking on a deep orange colour. After evaporation of the ethanol *in vacuo*, 10% aqueous NH$_4$PF$_6$ (*ca*. 5 mL) was added to the aqueous solution and the resulting orange suspension was washed with 10 mL portions of DCM until the organic layer no longer took on an orange colour. The combined organic layers were dried *in vacuo* yielding an orange solid (107 mg) containing a mixture of part-hydrolysed [Et$_4$**2**]$^{2+}$ and [(Et$_4$dpbpy)$_2$Ru(5-crown-phen)]$^{2+}$ derivatives. These were re-esterified by refluxing for 5 hours in triethylorthoacetate (3 mL), with sufficient anhydrous acetonitrile added to allow complete dissolution of the starting material. The crude product was precipitated with diethyl ether and columned over silica (eluent 80:8:1 then 40:8:1 acetone/H$_2$O/satd. KNO$_3$). Acetone was removed *in vacuo* from the second orange band, containing [Et$_4$**2**]$^{2+}$, and addition of aqueous NH$_4$PF$_6$ afforded a precipitate which was filtered off, washed with water and dried. Reprecipitation from acetone/diethyl ether in the presence of 18-crown-6 gave an orange solid: 32 mg, 0.021 mmol, 23%; δ_H (300 MHz, (CD$_3$)$_2$CO) 9.15 (2 H, d, *J* = 13.2 Hz, C$_5$H$_3$PN), 8.91 (2 H, d, *J* = 8.5 Hz, C$_5$H$_3$N), 8.82 (2 H, d, *J* = 8.5 Hz, C$_5$H$_3$N), 8.46 (2 H, d, *J* = 5.1 Hz, C$_5$H$_3$N), 8.21 (2 H, dd, *J* =5.7 Hz, 4.0 Hz, C$_5$H$_3$PN), 8.12 (2 H, d, *J* = 5.3 Hz, C$_5$H$_3$N), 7.89 (2 H, dd, *J* = 8.5 Hz, 5.3 Hz, C$_5$H$_3$N), 7.72 (2 H, dd, *J* = 8.3 Hz, 5.1 Hz, C$_5$H$_3$N), 7.63 (2 H, dd, *J* = 12.5 Hz, 5.7 Hz), 4.66–4.48 (8 H, m, CH$_2$), 4.28–3.98 (16 H, m, CH$_2$), 3.80 – 3.62 (16 H, m, CH$_2$), 1.29 (12 H, *p*q, *J* = 7.4 Hz, CH$_3$). ESI$^+$-MS: *m/z* 1415.3 [Et$_4$**2**+PF$_6$]$^+$, 635.17 [Et$_4$**2**]$^{2+}$. FTIR (diamond anvil) cm^{-1}: 2911 w, 2856 w, 1733 vw, 1623 m, 1599 vw, 1583 vw, 1513 vw, 1464 m, 1428 m, 1397 m, 1342 m, 1321 m, 1256 m, 1123 s, 1077 s, 1048 s, 1015 s, 975 m, 832 vs, 727 m, 556 vs. Elemental analysis for C$_{58}$H$_{70}$F$_{12}$N$_6$O$_{16}$P$_4$Ru ([Et$_4$**2**][PF$_6$]$_2$) calcd (found) %: C 44.65 (44.56), H 4.52 (4.58), N 5.39 (5.26). Note: a significant quantity of the mono-crown product [Et$_8$**3**](PF$_6$)$_2$ was isolated from the first orange band: 12 mg, 0.0074 mmol, 10%; δ_H (300 MHz, (CD$_3$)$_2$CO) 9.14 (2 H, d, 13.4 Hz, C$_5$H$_3$PN), 9.12 (2 H, d, *J* = 13.4 Hz, C$_5$H$_3$PN), 8.90 (2 H, d, *J* = 8.5 Hz, C$_5$H$_3$N), 8.41–8.36 (2 H, m, C$_5$H$_3$PN), 8.34 (2 H, d, *J* = 5.3 Hz, C$_5$H$_3$N), 8.08–8.04 (2 H, m, C$_5$H$_3$PN), 7.86 (2 H, dd, *J* = 8.5 Hz, 5.3 Hz, C$_5$H$_3$N), 7.76 (2 H, dd, *J* = 12.5 Hz, 5.7 Hz, C$_5$H$_3$PN), 7.60 (2 H, dd, *J* = 12.5 Hz, 5.7 Hz, C$_5$H$_3$PN), 4.63–4.52 (4 H, m, CH$_2$), 4.27–4.08 (16 H, m, CH$_2$), 4.07–4.03 (4 H, m, CH$_2$), 3.78–3.67 (8 H, m, CH$_2$), 1.36–1.24 (24 H, m, CH$_3$). ESI$^+$-MS: *m/z* 1473.28 [M+PF$_6$]$^+$, 664.15 [M]$^{2+}$. FTIR (diamond anvil) cm^{-1}: 2984 w, 2910 w, 1733 vw, 1623 m, 1599 vw, 1583 vw, 1513 vw, 1464 m, 1429 m, 1397 m, 1342 w, 1322 w, 1252 m, 1125 m, 1078 m, 1048 s, 1014 s, 978 m, 832 vs, 727 m, 556 vs. Elemental analysis for C$_{56}$H$_{74}$F$_{12}$N$_6$O$_{17}$P$_6$Ru, calcd (found) %: C 41.57 (41.44), H 4.61 (4.51), N 5.19 (5.15).

Synthesis of [(H$_2$dpb)Ru(5-crown-phen)$_2$] ([H$_2$2]). [Et$_4$**2**][PF$_6$]$_2$ (85 mg, 0.055 mmol) was suspended in 4.0 M aqueous HCl and refluxed for 4 hours before evaporation to dryness *in vacuo*. The resulting red solid was chromatographed on Sephadex LH20 resin, with H$_2$O as eluent. The collected orange fractions were reduced in volume *in vacuo* and precipitation by addition of acetone yielded red, solid [H$_2$**2**]•11H$_2$O: 41 mg, 0.031 mmol, 56%; δ_H (400 MHz,

D_2O) 8.78–8.69 (4 H, m, C_5H_3PN + C_5H_3N), 8.64 (2 H, d, *J* = 8.2 Hz, C_5H_3N), 8.15 (2 H, d, *J* = 5.2 Hz, C_5H_3N), 7.84 (2 H, d, *J* = 5.2 Hz, C_5H_3N), 7.78 (2 H, dd, *J* = 5.5 Hz, 3.6 Hz, C_5H_3PN), 7.71 (2 H, dd, *J* = 8.5 Hz, 5.2 Hz, C_5H_3N), 7.51 (2 H, dd, *J* = 8.2 Hz, 5.2 Hz, C_5H_3N), 7.42 (2 H, dd, *J* = 11.6 Hz, 6.1 Hz, C_5H_3PN), 4.49–4.42 (8 H, m, CH_2), 4.09 – 4.02 (8 H, m, CH_2), 3.83–3.74 (16 H, m, CH_2). ESI$^+$-MS: *m/z* 1179.2 ([H_2**2**-Na]$^+$), 1168.2 ([(H_2**2**)$_2$HNa]$^{2+}$), 1157.2 ([H_3**2**]$^+$). FTIR (diamond anvil) cm^{-1}: 3375 s, 3240 s, 3081 m, 2866 m, 1643 w, 1620 m, 1597 w, 1580 w, 1461 m, 1426 m, 1397 m, 1339 m, 1317 m, 1266 w, 1238 m, 1176 w, 1119 s, 1075 s, 1049 s, 973 w, 908 m, 811 m, 719 m. Elemental analysis for $C_{50}H_{78}N_6O_{27}P_2Ru$ (**[**H_2**2**]•11H_2O) calcd (found) %: C 44.35 (44.20), H 5.51 (5.42), N 6.21 (6.21).

Synthesis of [NBu_4]$_7H_3$[{$Ru_4O_4(OH)_2(H_2O)_4$}γ-$SiW_{10}O_{36}$)$_2$] (TBA_7H_3[1]). $Rb_8K_2[Ru_4O_4(OH)_2(H_2O)_4(SiW_{10}O_{36})_2]$•25$H_2O$ (57 mg, 8.54 μmol) was dissolved in water (10 mL). Excess solid NBu_4NO_3 (1.00 g, 3.29 mmol) was added, resulting in precipitation of a dark brown solid. This was recovered by filtration, washed with H_2O (3 × 10 mL) and air dried, before reprecipitation from MeCN/Et_2O yielded TBA_7H_3**[1]**•5H_2O as a dark brown solid (43 mg, 69%). FTIR (KBr disc) ν cm^{-1}: 3447 m, 2962 s, 2874 m, 1636 m, 1484 m, 1380 m, 1152 w, 1108 w, 1062 w, 1009 w, 967 s, 919 vs, 883 s, 803 vs, 764 sh, 549 w. UV-vis (MeCN), λ nm (ε 10^3 M^{-1} cm^{-1}): 269 (98.6), 460 (22.2). Elemental analysis for $C_{112}H_{275}N_7O_{87}Ru_4Si_2W_{20}$ (TBA_7H_3**[1]**•5H_2O) calcd (found) %: C 18.53 (18.22), H 3.82 (3.63), N 1.35 (1.51). TGA indicates a 2.2% mass loss by 200 °C (calcd 2.2% for H_2O).

12.2 X-Ray Crystal Structure Determination

Suitable single crystals of H_2**2**•C_2H_6O•8H_2O were obtained by vapour diffusion of acetone into an aqueous solution of H_2**2**. A crystal was selected under ambient conditions, mounted on a cryoloop using Paratone-N oil, and placed under the cryostream at 173 K. Crystal evaluation and collection of X-ray diffraction intensity data were performed using a Bruker Apex II CCD diffractometer (Cu K_α, λ = 1.54178 Å), and data reduction was carried out using the Bruker *APEXII* program suite.[9] Correction for incident and diffracted beam absorption effects were applied using empirical methods.[10] H_2**2**•C_2H_6O•8H_2O crystallized in the space group *Pnna* as determined by systematic absences in the intensity data, intensity statistics and the successful solution and refinement of the structure. Structure solution and refinement was carried out using the Bruker SHELXTL software package.[11] The structure was solved by direct methods and refined against F^2 by the full matrix least-square technique. All non-H atoms were refined anisotropically and H atoms were included in calculated positions, H-atoms on the -PO_3H groups and included water could not be located and refined. The C-C distance in the included acetone molecule was restrained. The final CIF file was validated using the IUCr CheckCIF online service. Crystal data, data collection parameters and refinement statistics are listed in Table S4, bond lengths and angles in Table S1.

Table S4 Crystal Data, Data Collection Parameters and Refinement Statistics for **$H_2$2**•C_2H_6O•$8H_2O$

Empirical formula	**$C_{53}H_{69}N_6O_{25}P_2Ru$**
F_w / g mol^{-1}	1353.15
T / K	173(2)
λ / Å	1.54178
Crystal system	Orthorhombic
Space group	*Pnna*
a / Å	21.3561(4)
b / Å	19.4016(3)
c / Å	14.9635(2)
α / °	90
β / °	90
γ / °	90
V /Å^3	6200.0(2)
Z	4
ρ_{calc} / g cm^{-3}	1.450
μ / mm^{-1}	3.271
Crystal size / mm^3	0.80 × 0.20 × 0.20
No. reflections (unique)	50722 (5616)
R_{int}	0.0385
θ_{max}	69.17
Completeness to θ_{max}	96.8%
Data / restraints / parameters	5616 / 1 / 404
Goodness-of-fit on F^2	1.108
Residuals: R_1; $wR2$[a]	0.0680; 0.1922
Final difference peak and hole / eÅ^{-3}	1.000; –0.704

[a] $R_1 = \Sigma||F_o| - |F_c||/\Sigma|F_o|$. $wR_2 = \{\Sigma[w(F_o^2 - F_c^2)^2]/\Sigma[w(F_o^2)^2]\}^{1/2}$.

12.3 Laser Photophysical Measurements

Ultrafast Visible Transient Absorption. The femtosecond transient absorption spectrometer is based on a regeneratively amplified Ti:sapphire laser system (coherent Legend, 800 nm, 150 fs, 3 mJ/pulse and 1 kHz repetition rate) and a Helios spectrometer (Ultrafast Systems LLC). The excitation pulse at 400 nm was generated by doubling the frequency of the fundamental 800 nm pulse using a β-barium borate (BBO) type I crystal. The energy of the 400 nm pump pulse was set to ~250 nJ/pulse with a neutral density filter. The pump beam diameter at the sample was ~400 µm, corresponding to an excitation density of ~2 µJ/cm^2 per pulse. A white light continuum (WLC) (450~720 nm), used as a probe, was generated by attenuating and focusing 10 µJ of the fundamental 800 nm pulse into a sapphire window. This WLC was split in two parts used as a probe and reference beams. The probe beam was focused with an aluminium parabolic reflector into the sample with a beam diameter of ~150 µm. The reference and probe beams were focused into a fiber-coupled multichannel spectrometer with CMOS sensors and detected at a frequency of 1 kHz. To minimize low-frequency laser fluctuations every other pump pulse was blocked with a synchronized chopper (New Focus Model 3501) at 500 Hz, and the absorbance change was calculated with two adjacent probe pulses (pump-blocked and pump-unblocked). The delay between the pump and probe pulses was controlled by a motorized translational stage. Samples were mounted on a stage and constantly moved by a controller throughout the measurements to avoid the destruction of samples. In all transient absorption spectra, the chirp and time zero correction were performed with Surface Explorer software (v.1.1.5, Ultrafast Systems LCC). The typical instrument response of our spectrometer is well represented by a Gaussian function with a full width at half-maximum (FWHM) of 180 ± 10 fs.

Nanosecond Transient Absorption. Measurements at the ns to μs timescales were carried out in an EOS spectrometer (Ultrafast Systems LLC). The pump pulses at 400 nm were generated from the same laser system described above. The probe pulse, a 0.5 ns white-light source operating at 20 kHz, was synchronized with the femtosecond amplifier, and the delay time was controlled by a digital delay generator. The probe light was detected in a fiber-optic-coupled multichannel spectrometer with a complementary metal−oxide−semiconductor (CMOS) sensor. The absorbance change was calculated from the intensities of sequential probe pulses with and without the pump.

Ultrafast Visible Pump/IR Probe Transient Absorption. Our tunable femtosecond infrared spectrometer is based on a Clark IR optical parametric amplifier (OPA) which generates two tunable near-IR pulses in the 1.1 to 2.5 μm spectral range (signal and idler, respectively). The broad mid-IR pulses centered at 2000 cm^{-1} were generated by difference frequency generation (DFG) combining the corresponding signal and idler in a 1-mm-thick type II $AgGaS_2$ crystal. Frequency tuning of the mid-IR pulses was achieved by changing the signal and idler frequencies at the OPA and optimizing the timing between the pulses and the phase matching angles of the BBO (OPA crystal) and the $AgGaS_2$ crystal. After difference frequency generation, the mid-IR pulse was collimated and split in two parts with a 90% beam splitter. The 10% transmitted part was used as a probe in the visible pump-IR probe transient absorption measurements. To prevent cumulative heating in the sample and to avoid the saturation of the detector, the intensity of the probe mid-IR pulse was attenuated using neutral density filters to approximately 40 μJ, before it was focused into a 0.4 μm CaF_2 path-length cell containing the sample. At the focal point, the probe was spatially overlapped with the temporally delayed 400 nm with a pump beam with energy of about 2 μJ per pulse. To avoid rotational diffusion effects, the polarization angle of the excitation beams were controlled with a half-wave plate and set to the magic angle (54.7°) relative to the probe beam. The diameter of the pump and probe beams were 400 and 200 μm, respectively. The mid-infrared probe pulse was spectrally dispersed with an imaging spectrograph (CVI, Digikrom 240) and imaged onto a 32-element infrared HgCdTe (MCT) array detector. The difference absorption spectra were calculated by subtracting the absorption spectrum of the excited sample from the absorption spectrum of the sample in the ground state by blocking every other pump pulse with a phase-locked optical chopper (New Focus) at 500 Hz. The instrument response function of our spectrometer was well represented by a Gaussian function with a 230 ± 10 full width at half-maximum (FWHM) for the VIS-IR setup.

12.4 Photoelectrochemistry

Set-Up. A long (*ca.* 6 cm) FTO slide with a *ca.* 1.4 cm^2 ds-TiO_2 film was attached to some self-adhesive copper tape. A similar length platinized FTO film (Pt@FTO), also attached to self-adhesive copper tape, was then taped to this photoanode, with a *ca.* 1 mm thick spacer separating the two working surfaces (Figure S20). The sides of the assembly were sealed using Paraffin wax (we found Nair™ hair removal wax to be excellent for this purpose), leaving the bottom open for ingress of gas. The copper tape was connected to crocodile clips fed through a rubber stopper and the assembly inserted into the flat-fronted working compartment of a two compartment electrochemical cell which was then evacuated and back-filled with Ar. Degassed buffer was introduced by syringe and the reference and counter electrodes, connected to another rubber stopper with electrochemical feed-throughs, were introduced to the cell while under a constant stream of Ar. The entire assembly was degassed

for a further 5 to 10 minutes and the measurement performed under a slow, constant stream of Ar to prevent ingress of atmospheric O_2. Using a bipotentiostat, the generator electrode was set to a bias potential of 0 mV *vs* Ag/AgCl, and the detector to -0.516 V (pH 5.8) or -0.600 V (pH 7.2). In some cases the background was reduced before measurement by running the detector for several periods of 60 s.

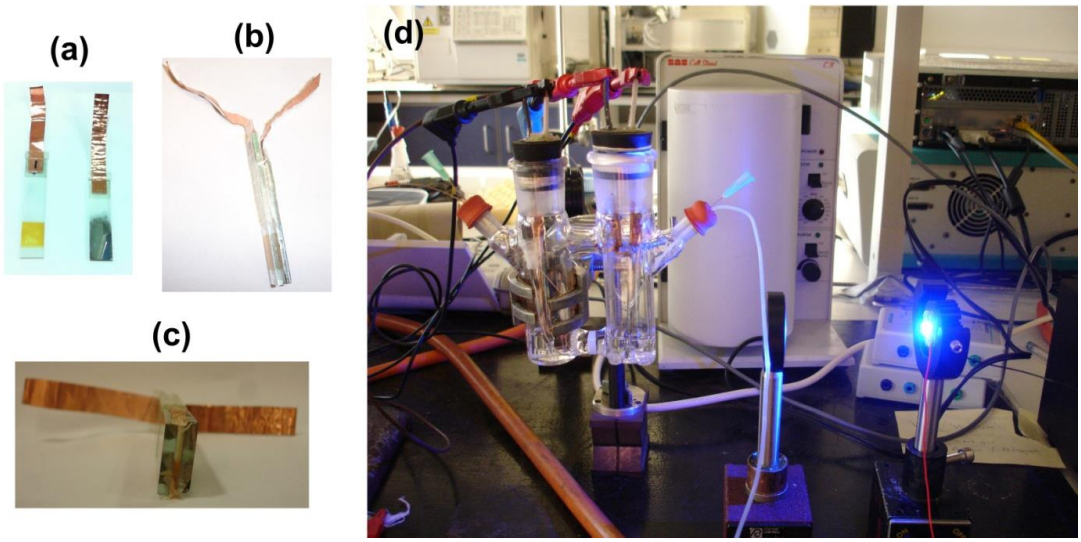

Figure S20 The photoelectrochemical generator/detector set up: **(a)** Photoanode (left) and Pt@FTO detector (right) electrodes connected to copper tape; **(b)** Photoanode and detector taped together with *ca*. 1mm spacing; **(c)** End view showing sealing of sides with wax and opening at the bottom for buffer ingress; **(d)** Photoelectrochemical cell under illumination with constant Ar purge.

Detector Calibration. The following procedure was used, which assumes that Pt@FTO has near 100% faradaic efficiency for oxygen evolution:

Two Pt@FTO films were held together, spaced by *ca.* 1 mm. The bipotentiostat was run with the generator at 0 mV, and the collector at the desired collector potential (-0.516 V at pH 5.8, -0.600 V at pH 7.2) for 180 s to achieve a steady background (Figure S21) current. Then the potential of the generator was stepped to +1.2 V (pH 5.8) or + 1.1 V (pH 7.2) for 360 s. To ensure measurement of faradaic currents, the generator and collector currents (I_g and I_c) were measured after 120 s. The collector efficiency was then calculated as follows:

Collector efficiency = ($|I_c$ - background|)/($|I_g$ – background|)

Over many calibration runs, this was consistently *ca.* 60% at both pHs.

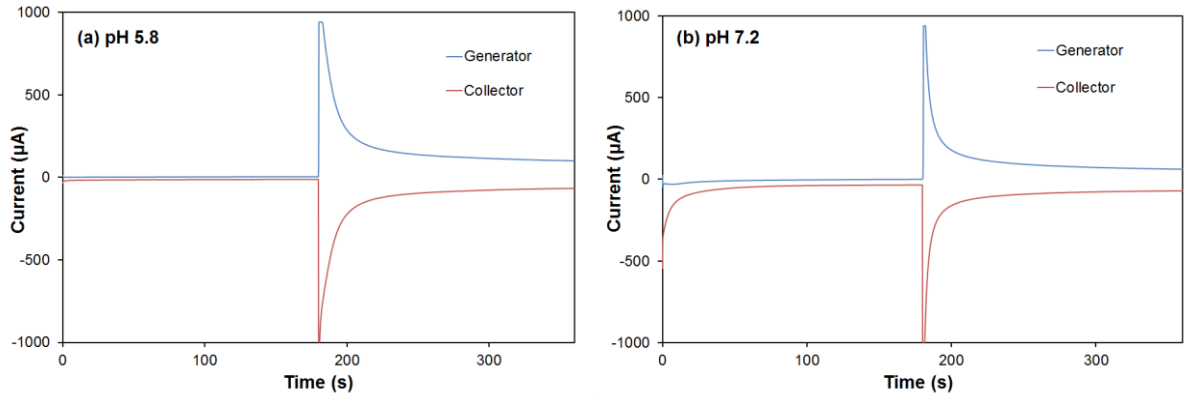

Figure S21 Calibration experiments for the generator – collector assembly: **(a)** In pH 5.8 Na_2SiF_6/$NaHCO_3$ (with $NaClO_4$ added so that [Na^+] = 200 mM), generator at +1.2 V, collector at -0.516 V; **(b)** In pH 7.2 lutidine (200 mM $NaClO_4$ electrolyte), generator at + 1.1 V, collector at -0.600 V.

Detector background determination in PEC measurements. A challenge in the photoelectrochemical measurements is correctly determining the detector background. If a Pt@FTO film with adequate sensitivity is used, the background signal is often similar or greater in magnitude than the measurement signal and tends to slope down as background O_2 is consumed. To estimate the background at the end of the transient, we took an average of the background immediately before the transient (*i.e.* 60 s before the end of the transient), and immediately before the next transient (60 s after the end of the transient) – in other words assuming a linear decay between the two points. This typically overestimates the background, and hence slightly underestimates faradaic efficiency. In some cases with low photocurrents and hence low collector currents (TiO_2-**P2** dyads), this underestimation of faradaic efficiency was severe enough that we instead used the current 60 s after the end of the transient alone to provide a background, likely leading to slight overestimates of faradic efficiency.

13. References

1 (a) A. Zaban, S. Ferrere, J. Sprague and B. A. Gregg. *J. Phys. Chem. B* 1997, **101**, 55. (b) C. X. She, J. C. Guo, S. Irle, K. Morokuma, D. L. Mohler, H. Zabri, F. Odobel, K. T. Youm, F. Liu, J. T. Hupp and T. Lian, *J. Phys. Chem. A* 2007, **111**, 6832.

2 Y. V. Geletii, B. Botar, P. Kögerler, D. A. Hillesheim, D. G. Musaev and C. L. Hill, *Angew. Chem. Int. Ed.* 2008, **47**, 3896.

3 X. Xiang, J. Fielden, W. Rodríguez-Córdoba, Z. Huang, N. Zhang, Z. Luo, D. G. Musaev, T. Lian and C. L. Hill, *J. Phys. Chem. C* 2013, **117**, 918.

4 C. R. Rice, A. Guerrero, Z. R. Bell, R. L. Paul, G. R. Motson, J. C. Jeffery, M. D. Ward, *New. J. Chem.* 2001, **25**, 185.

5 V. Penicaud, F. Odobel and B. Bujoli, *Tetrahedron Lett.* 1998, **39**, 3689.

6 (a) M. Montalti, S. Wahdwa, W. Y. Kim, R. A. Kipp and R. H. Schmehl, *Inorg. Chem.* 2000, **39**, 76. (b) I. Gillaizeau-Gauthier, F. Odobel, M. Alebbi, R. Argazzi, E. Costa, C. A. Bignozzi, P. Qu and G. J. Meyer, *Inorg. Chem.* 2001, **40**, 6073.

7 I. P. Evans, A. Spencer and G. Wilkinson, *J. Chem. Soc., Dalton Trans.* 1973, 204.

8 C. H. Yoon, R. Vittal, J. Lee, W.-S. Chae, K.-J. Kim, *Electrochimica Acta*, 2008, **53**, 2890.

9 APEXII (Version 2.0-1), SAINT (Version 7.23A) and SADABS (Version 2004/1), Bruker AXS Inc.: Madison, WI, USA, 2005.

10 R. H. Blessing, *Acta Crystallogr.* 1995, **A51**, 33.

11 SHELXTL (v 6.1), Bruker AXS Inc.: Madison, WI, USA, 2000.